*eng*

MDPI

*Article*

# On the Importance of Solar Radiation and Shading for the Alkali–Aggregate Reaction Prediction of Concrete Arch Dams

**Noemi Schclar Leitão**

Laboratório Nacional de Engenharia Civil (LNEC), Av. do Brasil, 101, 1700-066 Lisbon, Portugal; nschclar@lnec.pt

**Abstract:** The environmental conditions to which dams are exposed play a major role in dictating the progression and manifestation of the alkali–aggregate reaction (AAR). However, in the numerical thermal-mechanical simulation of AAR-affected dams, the solar radiation and its associated shadow effects have received little attention. The spatiotemporal distribution of the solar radiation incidence on the dam surfaces has often been addressed in a simplified way or has just been neglected. Yet, far less attention has been given to shadows cast by the dam's own geometry or the slopes. The main reasons for these simplifications derive from the fact that contrary to other thermal loads, environmental actions vary in daily and annual cycles, with the added complication that solar radiation also depends on the orientation of the surface with respect to the Sun's rays. In this way, a conventional thermal finite element code should be modified in order to deal with these two particular issues. Therefore, this article starts with the estimation of the solar radiation distribution by recourse to concepts of astronomy and computer graphics. Then, to illustrate the influence of the nonuniform temperature distribution on dam surfaces due to solar radiation and shading, the analysis of an AAR-affected arch dam is presented in this paper. A comparison of the AAR expansions computed on the dam with or without considering the solar radiation and shading is presented.

**Keywords:** solar radiation; shadow; alkali–aggregate reaction; concrete dams; finite elements



**Citation:** Leitão, N.S. On the Importance of Solar Radiation and Shading for the Alkali–Aggregate Reaction Prediction of Concrete Arch Dams. *Eng* **2024**, *5*, 1673–1695. https://doi.org/10.3390/eng5030088

Academic Editors: Thaiyal Naayagi Ramasamy, F. Pacheco Torgal, Iolanda De Marco and Valentina Di Pasquale

Received: 19 June 2024
Revised: 19 July 2024
Accepted: 26 July 2024
Published: 1 August 2024



## 1. Introduction

A significant number of concrete dams built mainly before the mid-20th century have been affected by alkali–aggregate reactions (AARs) around the world. An AAR is a chemical reaction that occurs between the alkali hydroxides provided mainly by Portland cement and certain types of reactive silica minerals present in some aggregates. It can lead to the development of several cracking over decades as a consequence of internal expansions, sometimes accompanied by the appearance of efflorescence and exudations on the faces of the dam. This reaction does not represent a potentially catastrophic or rapid failure issue for dams [1]. By contrast, an AAR is a slowly developing mechanism that can cause significant degradation in the mechanical properties of the concrete leading to a considerable reduction in its ability to resist other loads. In the extreme, the advanced state of degradation caused by the AAR can lead to the demolition of the dam and its substitution for a new one.

The environmental conditions to which the dam is exposed play a major role in dictating the progression and manifestation of this reaction [2]. The effect of temperature on the rate of silica dissolution, which is a critical process in the development of AARs, has been extensively reported. Warmer average temperatures in general will accelerate silica dissolution and the subsequent formation of an AAR gel.

Amberg et al. [3], analyzing the behavior of Swiss dams affected by AARs, concluded that radiant heat significantly influenced swelling behavior. They observed that gravity dams tend to drift towards the north due to the greater expansion experienced by the face exposed southward, which receives more solar insolation.

Arch dams, instead, always move upstream due to AAR expansion [4]; but as the rise in temperature due to solar radiation depends on the slope and orientation of the exposed surface, the rate of expansion differs from one point to another, remaining highest in the zones that receive more solar insolation.

However, in the numerical thermal-mechanical simulation of AAR-affected dams, the solar radiation and its associated shadow effects have received little attention. The spatiotemporal distribution of the solar radiation incidence on the dam surfaces has often been addressed in a simplified way or has just been neglected. Yet, far less attention has been given to shadows cast by the dam's own geometry or the slopes.

For the diagnosis of AARs in the Isola arch gravity dam, Saouma and co-workers [5,6] introduced the effect of solar radiation by modifying the upstream and downstream air temperature. In the case of the Pian Telecoil arch gravity dam, also suffering from the effects of AARs, Stucchi and Catalano [7] calculated the dam temperature using the one-dimensional algorithm given in [8], in which the interior temperature was calculated from the measured temperatures at upstream and downstream faces of the dam. In this way, the solar radiation was implicitly considered from the measured surface temperatures. Lamea and Mirzabozorg [9], instead, introduced the solar radiation effect in an explicit manner in the assessment of the Dez double curvature arch dam. However, these authors did not consider the self- and external shadows, although the dam has a height of 203 m and is located in a steep-sided valley. Moreover, it was not clear if the dam was effectively affected by AAR expansion or it was an academic example, since no comparison between computed and observed values was presented.

The main reasons for these simplifications derive from the fact that contrary to other thermal loads, environmental actions vary in daily and annual cycles, with the added complication that solar radiation also depends on the orientation of the surface with respect to the Sun's rays. Moreover, to compute the solar radiation that reaches the surfaces of the dam, concepts of astronomy and computer graphics must be incorporated in the finite element analysis. In this way, a conventional thermal finite element code should be modified in order to deal with these two particular issues.

Following previous work presented by the author and coworkers [10,11], the solar radiation effect and the shading are considered in this article.

In the present study, the Alto Ceira dam was selected in order to evaluate the influence of the solar radiation and the shadow effects in the development of AAR expansion. During all its service life, the AAR expansion led to irreversible vertical and horizontal deformations, which never showed signs of slowing down. From the beginning, the observed deformation revealed an uneven distribution along the dam with the largest deformation registered on the right side, which corresponded to the side receiving a greater amount of annual solar insolation. In 1995, using the displacements measured from 1950 to 1993, a 3D finite element back analysis was performed in order to estimate the swelling strains which would cause those displacements [12,13]. However, regardless of how close the monitored and computed displacements were, this simplified approach did not allow researchers to gain neither new knowledge nor a deep understanding of the various phenomena that could influence or affect the AAR expansion. In this study, instead, a complete thermal-mechanical analysis is presented. In this way, the solar radiation or its occlusion is explicitly represented in the thermal analysis, whereas the mechanical analysis introduces the AAR evolution through its kinetic law instead of using an imposed deformation as in the old analysis. In addition, and contrary to the old version, the new mechanical model explicitly represents the nonlinear behavior induced by the opening/closing of the contraction joints and the dam–foundation interface by using zero-thickness interface elements.

## 2. Dam Description

Alto Ceria dam, shown in Figure 1, is located in the center of Portugal at the headwaters of the Ceira River, a little downstream of the confluence of the Fornea river.

**Figure 1.** Downstream view of Alto Ceira dam.

Designed by Halcrow & Partners, its construction was completed in 1949. Its function was to divert the water of the river Ceira and of its tributaries to the reservoir of Santa Luzia dam.

The dam was a thin arch dam with a maximum height of 37 m above the riverbed, a crest length of 120 m, and a thickness between 1.5 m at the crest and 4.5 m at the base of the central cantilever (Figure 2). A masonry spillway was located on the right bank.

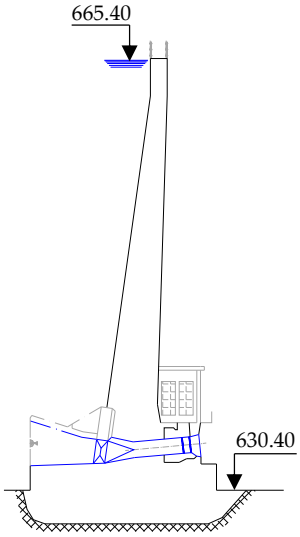


**Figure 2.** Central vertical cross section of Alto Ceira dam.

Shortly after it started its operation, a geodetic surveying system for monitoring absolute displacements of object points on the dam was implemented. The system was based on a separate horizontal and vertical control network: a triangulation network composed of nine object points on the downstream face of the dam and a geometric levelling line composed of seven object points on the crest of the dam, as it is shown in Figure 3.

Since its early lifetime, the dam began experiencing increasing movements in the upstream and upward directions, accompanied by extensive cracking especially concentrated in the flanks and on the crest. Figures 4 and 5 illustrate the evolution of the horizontal and vertical displacements measured between 1950 and 1986.

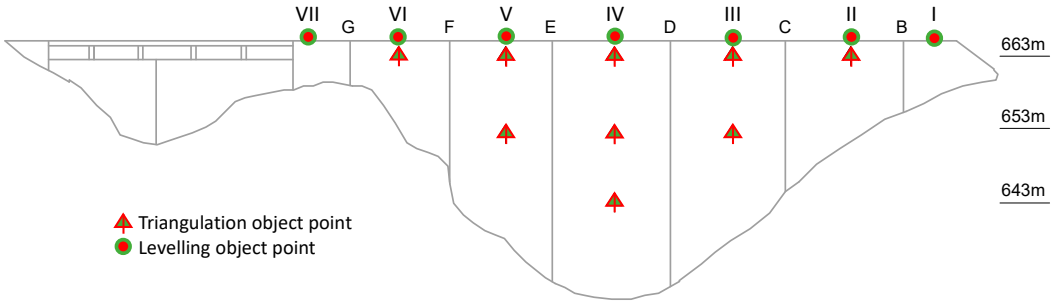


**Figure 3.** Downstream elevation view, geodetic surveying targets.

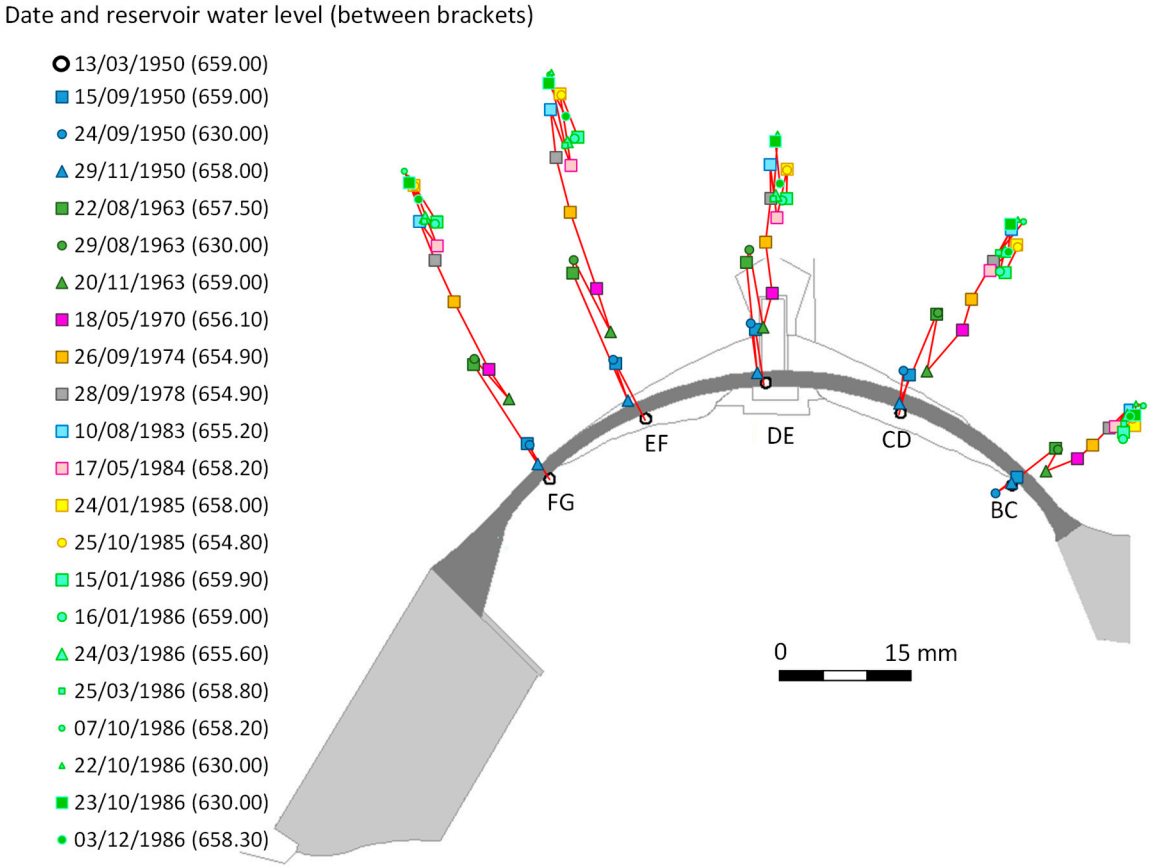


**Figure 4.** Horizontal displacements of the object points at level 663.0 m between 1950 and 1986.

From 1950 to 1978, geodetic measurements were carried out sporadically. The first two surveys, in 1950 and 1963, involved the emptying and subsequent filling of the reservoir, just for the sake of characterizing the behavior of the dam.

After that, three other surveys were conducted in 1970, 1974, and 1978. The comparison between the displacements obtained in the surveys from 1974 and 1978, carried out at the same time of the year and with the same reservoir water level, confirmed the tendency of the dam to experience anomalous increasing movements in the upstream and upward directions. This evidence led to the reduction in the time intervals between surveys to at least once per year.

In 1986, another emptying and filling of the reservoir was carried out in order to determine the source of the anomalous behavior experienced by the dam [13]. Numerous studies, including visual inspections, a mapping of cracks, core testing and a petrographic analysis of concrete samples, were carried out in order to identify the source of such expansion.

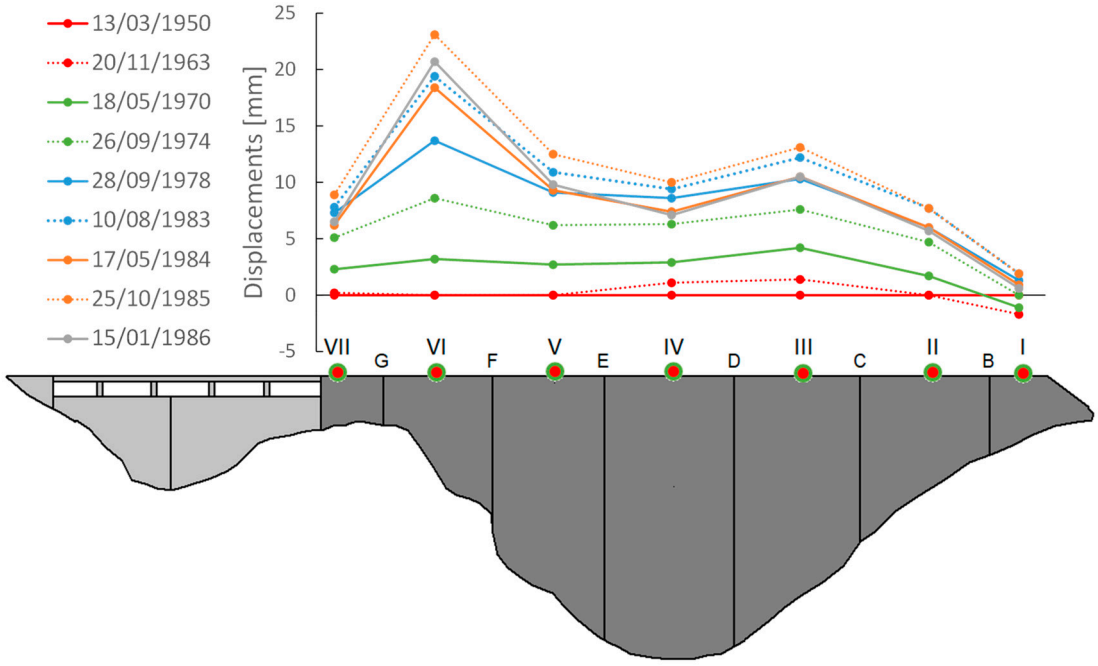


**Figure 5.** Vertical displacements of the object points on the crest between 1950 and 1986.

Laboratory testing on concrete cores allowed the researchers to conclude that alkali–silica reactions were responsible for the observed expansion, essentially due to reactive silica of cataclastic quartz and cryptocrystalline quartz, occurring between lamellas of quartzite and metapellites and alkalis, mainly potassium, from feldspars, namely, microcline [14].

For the computational modelling of the evolution of the damage and assessment of the structural response, two different finite element analyses considering the induced expansion as imposed deformation were performed in 1995 [13] and 2004 [15]. For these studies, the dam was a priori divided in different zones of constant swelling and the imposed deformation of each zone was determined based on the horizontal and vertical observed displacement by a back-analysis procedure. In order to take into account the anisotropic expansion behavior, the imposed deformations were considered in separated horizontal and vertical components.

Crack mapping surveys were performed in 1986, 1994, and 2001. These surveys allowed researchers to follow the progressive changes in cracking. Figure 6 shows the crack mapping survey performed in 2001, indicating the length, width, and location of the visible cracks [16].

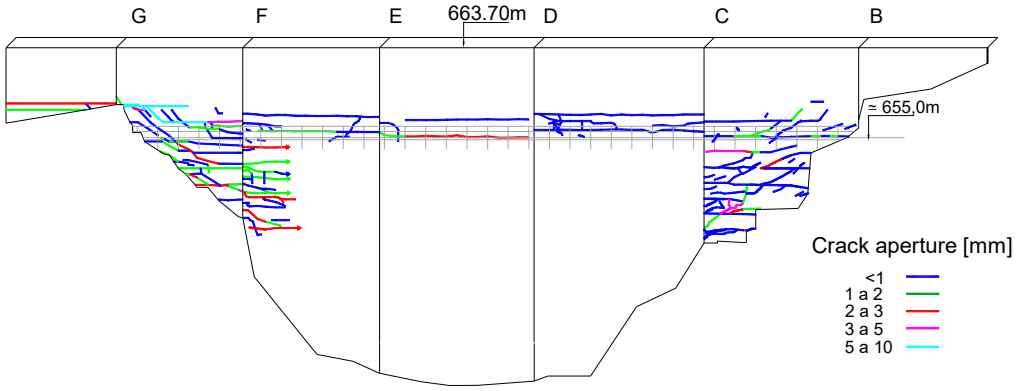


**Figure 6.** Crack mapping on the downstream face of the dam performed in 2001.

By the year 2006, the considerable depth reached by the cracks and the relatively intensive leakage through the dam body had begun to represent a threat to the safety of the dam. Since its rehabilitation was considered very difficult and expensive, it was decided to replace the affected dam with a new one. The new dam is located approximately 200 m downstream of the original one, which was partially demolished and submerged by the new reservoir in 2013.

## 3. Finite Element Model for the Thermal-Mechanical Analysis

The thermo-mechanical analysis was based on the finite element method involving two sequentially coupled analysis: a transient heat transfer analysis followed by a nonlinear static stress analysis. For practical reasons, the same finite elements mesh was used for both thermal and the mechanical analysis. For this purpose, the finite element model represented the concrete arch dam, the masonry spillway, and an appropriate volume of the foundation (Figure 7).

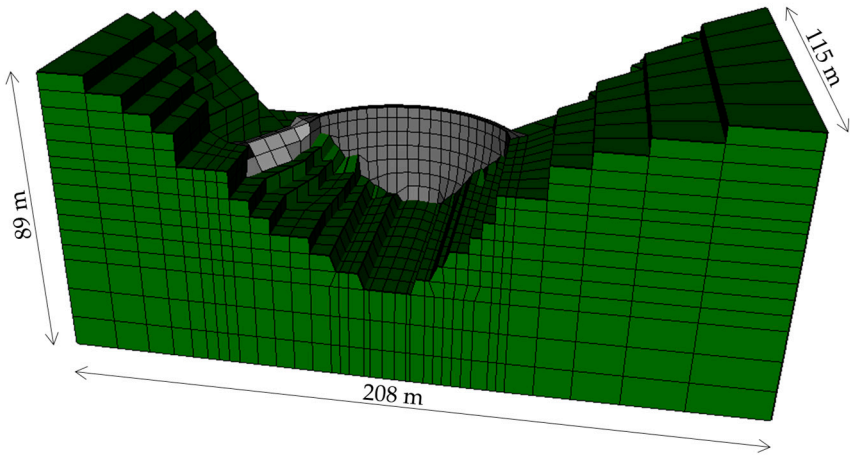


**Figure 7.** Finite element model of Alto Ceira dam.

The dam model comprised two layers of 20-node isoparametric solid elements through its thickness.

For the mechanical analysis, the arch was divided into seven blocks separated by radial vertical contraction joints. The contraction joints and the dam–foundation interface were represented by 16-node zero-thickness interface elements. In this way, the model was comprised of 3166 solid elements and 15,792 nodes for the thermal analysis, and 3166 solid elements, 124 interface elements, and 16,321 nodes for the mechanical analysis.

## 4. Thermal Analysis

### *4.1. General Remarks*

Seasonal variations in environmental actions strongly affect the behavior of concrete arch dams. During summer, the rise in temperature leads the dam to move upstream. During winter, the temperature decrease leads the dam to move downstream. These displacements usually are of the same size or larger than the displacements due to water level variation.

Moreover, if the dam is affected by an AAR, temperature, like in all other chemical reactions, influences the evolution of this reaction. In general, the rate of reaction and formation of gel increase as the temperature rises.

Despite their great influence on the structural behavior, standards provide more comprehensive information about mechanical loadings than environmental actions. This results in a variety of different criteria for selecting the main phenomena involved in the thermal analysis. In this sense, Salazar et al. [17] remark that some phenomena have been considered in all relevant works published over the last decade, namely, the heat

exchange by convection and the water temperature applied at the upstream face of the dam. Other phenomena, instead, such as dam–air exchange fluxes due to solar (short-wave) and atmospheric (long-wave) radiation, reflected solar and atmospheric radiation, evaporation or night cooling, have received less attention or have simply been neglected.

As it was mentioned before, solar radiation has a great influence on the rate of AAR expansion. Therefore, in this paper, special attention was given to the modelling of the solar radiation and the occlusion of the Sun's rays due to the geometry of the dam or the slopes.

### *4.2. Governing Equations*

The heat flowing inside a dam and the heat entering and leaving the dam are governed by different mechanisms. The heat inside the dam moves by conduction and it is treated as the governing equation expressed by the heat conduction equation. The heat entering or escaping the dam moves by convection, radiation, or both, and it is usually considered as a boundary condition. In what follows, only the relevant equations and their variables are introduced. A full explanation of the fundamental equations for a transient heat conduction analysis can be found in any heat transfer textbook for undergraduate engineering students; for more details, the reader can refer to [18].

The transient heat conduction equation for a stationary medium is given by:

$$\frac{\partial}{\partial x}\left[k_x \frac{\partial T}{\partial x}\right] + \frac{\partial}{\partial y}\left[k_y \frac{\partial T}{\partial y}\right] + \frac{\partial}{\partial z}\left[k_z \frac{\partial T}{\partial z}\right] + G = \rho\, c \frac{\partial T}{\partial t} \tag{1}$$

with the following boundary conditions

$$T = \overline{T} \qquad \text{in } \Gamma_T \tag{2}$$

$$k_x \frac{\partial T}{\partial x}\, l + k_y \frac{\partial T}{\partial y}\, m + k_z \frac{\partial T}{\partial z}\, n + q_c + q_r + q_q = 0 \qquad \text{in } \Gamma_q \tag{3}$$

and the following initial condition

$$T = T_o \qquad \text{in } \Omega \text{ for } t = t_o \tag{4}$$

where $t$ is the time; $T$ is the temperature; $k_x$, $k_y$, and $k_z$ are the thermal conductivities; $G$ is the internally generated heat per unit of volume and time; $\rho$ is the material density; $c$ is the specific heat; $\overline{T}$ is the temperature at the boundary $\Gamma_T$; $q_c$ is the heat flux due to convection; $q_r$ is the heat flux due to atmospheric (long-wave) radiation and $q_q$ is the solar (short-wave) radiation at the boundary $\Gamma_q$; $l$, $m$, and $n$ are the direction cosines; and $T_o$ is the temperature at time $t_o$. It is worth noting that the convention in expression (3) is positive when heat flux flows outwards from the body.

The heat exchange by convection between the surface of the structure and the air depends on wind speed and air temperature. The heat gain or loss from a surface due to convection is given by Newton's law

$$q_c = h_c\,(T - T_a) \tag{5}$$

where $T_a$ is the air temperature, and $h_c$ is the convection heat transfer coefficient, which is a function of the wind speed.

The temperature difference between the surface of the structure and the air gives origin to electromagnetic radiation, which is measured by the Stefan–Boltzmann law

$$q_r = \varepsilon\, \sigma \left(T^4 - T_a^4\right) \tag{6}$$

where $\varepsilon$ is the emissivity of the surface, and $\sigma$ is the Stefan–Boltzmann constant given as $5.669 \times 10^{-8}$ W(m$^2$ K$^4$). When $T$ and $T_a$ are close, which is the case in civil engineering structures, it is possible to rewrite (6) in a quasi-linear form

$$q_r = h_r(T - T_a) \tag{7}$$

where $h_r$ is the radiation linear coefficient defined as follows

$$h_r = \varepsilon\, \sigma \left(T^2 - T_a^2\right)(T - T_a) \tag{8}$$

Combining the contribution of both heat transfer mechanisms, convection and radiation, it is possible to define a new coefficient called total thermal transmission coefficient, $h_t$. This new coefficient, in essence, is a convection heat transfer coefficient that is updated to consider radiation.

The solar radiation boundary condition is given by

$$q_q = a\ I_T \tag{9}$$

where $a$ is the absorption coefficient, and $I_T$ is the solar irradiance.

### *4.3. Thermal Properties and Boundary Conditions*

Due to the lack of information, the same thermal properties were adopted for the concrete and the rock mass. The conductivity was set to 2.62 W/(m K), the specific heat capacity to 920 J/(kg K), and the density to 2400 kg/m$^3$, which are within the typical range of values suggested by [19] for mass concrete.

Regarding the boundary conditions: convection and atmospheric and solar radiation actions were considered at the exposed surfaces of the dam, and a prescribed temperature corresponding to the reservoir water temperature was applied in all submerged boundaries. For the rock mass foundation: convection and atmospheric radiation boundary conditions were applied in all air-exposed boundaries; prescribed temperature corresponding to the reservoir water temperature boundary conditions were applied in all submerged boundaries; adiabatic boundary conditions were considered at the lateral boundaries; and a fixed temperature boundary condition of 13 °C was imposed at the bottom.

### *4.4. Convection Heat Transfer*

The daily air temperature was represented as the superposition of two harmonic functions, one of annual period and another with a one-day period:

$$T(d) = 12.8 + 7.4\cos\left[\frac{2\pi}{365}(d - 26.1)\right] + \frac{A(d)}{2}\cos[2\pi(d - 0.125)] \tag{10}$$

with

$$A(d) = 10.2 + 3.6\cos\left[\frac{2\pi}{365}(d - 8.9)\right] \tag{11}$$

where the parameters involved in these functions were calculated based on the daily air temperatures registered at the dam site using the least squares method.

The convection coefficient was set to 20 W/(m$^2$ K) while a constant value of 5 W/(m$^2$ K) was adopted for the linearized radiation coefficient. Therefore, a constant value for the total thermal transmission coefficient $h_t$ = 25 W/(m$^2$ K) was applied to the whole model.

### *4.5. Reservoir Water Temperature*

The water temperature of the reservoir was introduced as a prescribed temperature using the approximation given by Bofang [20]:

$$T^{water}(y,d) = T_m^{water}(y) - T_a^{water}(y)\ \cos\left\{\frac{2\pi}{365}[d - d_o(y)]\right\}\ \ [^\circ\mathrm{C}] \tag{12}$$

with

$$T_m^{water}(y) = 8.97 + 4.63\exp(-0.15\,y) \quad [^\circ\mathrm{C}] \tag{13}$$

$$T_a^{water}(y) = -8.5\exp(-0.095\mathrm{y}) \quad [^\circ\mathrm{C}] \tag{14}$$

$$d_o(y) = [2 - 2.35\exp(-0.24\,y)]\frac{365}{12} + 26.1 \quad [\mathrm{days}] \tag{15}$$

where $y$ is the depth of the water, $d$ is the fractional day of the year, and $T_m^{water}$, $T_a^{water}$, and $d_o$ are the annual mean temperature, the amplitude of annual variation, and the phase difference of water temperature at depth $y$. The parameters involved in these equations were estimated based on the water temperature measured at the new Alto Ceira II dam. The analysis was run for a constant water level of 660.00 m.

### *4.6. Solar Radiation*

#### 4.6.1. The Path of the Sun across the Celestial Sphere

Solar radiation that reaches the boundaries of the Earth's atmosphere is beam radiation, also known as direct radiation. This radiation travels directly from the Sun to any point on the Earth along a straight line connecting the Sun with the selected point on Earth. Upon passing through the Earth's atmosphere, some radiation gets scattered. As a result, any point on the Earth's surface is reached by both beam radiation and radiation scattered by the atmosphere. Beam radiation is strictly directional, while the scattered radiation reaches the Earth's surface from all directions. Any tilted surface (in reference to a horizontal one) on Earth is reached by not only beam and scattered radiation but radiation reflected by the Earth's surface and various objects located nearby.

For a better understanding of the paths of the Sun in the sky, one can imagine a celestial sphere with the Earth at its center and the Sun revolving around it (geocentric system). The location of any surface in reference to the Sun is determined with fundamental concepts of spherical geometry relating to the Earth's movement in relation to the Sun. The apparent motion of the Sun is caused by the combined effects of the rotation of the Earth around its proper axis and the translation around the Sun. Therefore, the angle at which the direct component of light will strike the Earth exhibits daily and yearly changes in east–west (E-W) and south–north (S-N) directions, respectively.

Figure 8 shows the apparent motion of the Sun and its position at solar noon at the equinoxes and solstices, relative to the base of the Alto Ceira dam.

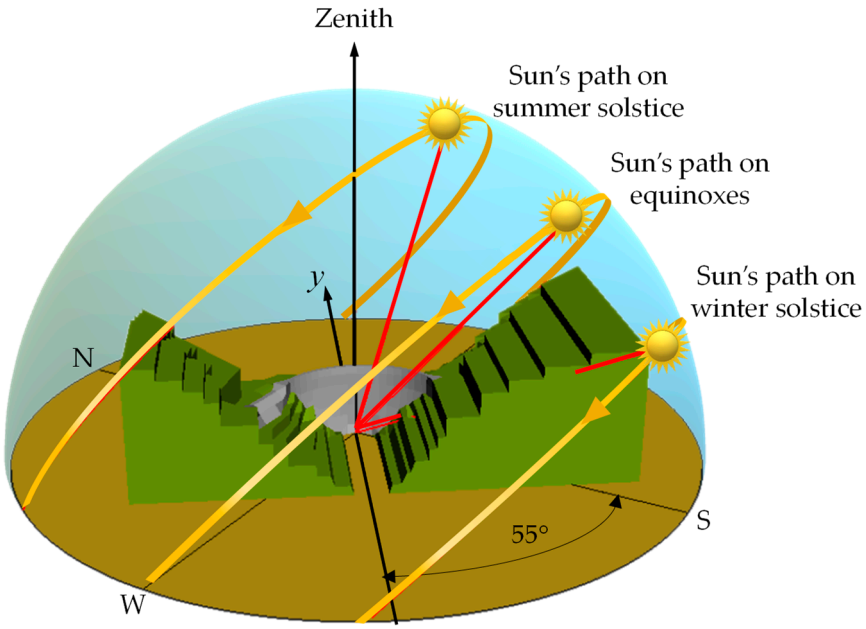


**Figure 8.** The Sun's paths across the sky as seen from the dam.

As can be seen in the figure, the Sun's path reaches its extreme excursions at the winter and summer solstices, around 22 December and 21 June, respectively, since the Alto Ceira dam is located in the northern hemisphere. At the solstices, the altitude at solar noon is decreased or increased by the inclination of the earth's axis (23°27′), respectively. At the equinoxes, around 21 March and 23 September, the Sun rises due east and sets due west, and at solar noon, the altitude equals 90° minus the latitude.

4.6.2. Solar Position

Before describing the equations that govern the solar flux, it is important to note that the time used in these equations is the apparent solar time $AST$, which directly tracks the diurnal motion of the Sun. Meanwhile, the chronological time that clocks use, called local standard time $LST$, corresponds to a certain time zone, in which noon does not necessarily correspond to the time when the Sun is highest in the sky. Additionally, the Earth does not rotate perfectly, rather, it wobbles on its axis creating what is known as an analemma. Therefore, to convert between local standard time and apparent solar time involves the equation of time $ET$ and a longitude correction, which corresponds to four minutes of time per degree difference between the local longitude $LON$ and the longitude of the local standard meridian $LSM$ for the time zone [21]:

$$AST = LST + \frac{ET}{60} + \frac{LON - LSM}{15} + Day\ saving \tag{16}$$

with

$$ET = 0.0075 + 0.1868\cos\gamma - 3.2077\sin\gamma - 1.4615\cos 2\gamma - 4.089\sin 2\gamma \tag{17}$$

where $\gamma = \frac{2\pi}{365}(N-1)$, where $N$ is the day of the year considering a year with 365 days, and $Day\ saving$ is either 0 or 1 h, depending on whether daylight saving time is applied.

The solar hour angle converts the solar time $AST$ into the number of degrees that the Sun moves across the sky. By definition, the solar hour angle is 0° at solar noon. Since the Earth rotates 15° per hour, each hour away from solar noon corresponds to an angular motion of the Sun in the sky of 15°. In the morning, the solar hour angle is negative; in the afternoon, the solar hour angle is positive:

$$\omega = 15(AST - 12) \tag{18}$$

While the Earth orbits the Sun, its axis is constantly tilted at 66°33′ to the orbit plane. Seasonal changes in the mutual location of the Earth and the Sun are described by the parameter known as the Sun's declination $\delta$. The declination is defined as the angle between the line connecting the Earth and the Sun, and the equatorial plane at solar noon. It can be represented by Spencer's formula, given by [22]:

$$\begin{aligned}\delta = 0.006918 - 0.399912\cos\gamma + 0.070257\sin\gamma - 0.006758\cos 2\gamma \\ +0.000907\sin 2\gamma - 0.002697\cos 3\gamma + 0.00148\sin 3\gamma\end{aligned} \tag{19}$$

The Sun position is described by two angles: the solar altitude above the horizontal, $\alpha_s$, and the solar azimuth measured from the south, $\psi_s$. Both angles are a function of the Sun's declination $\delta$, the earth's latitude $\phi$, and the solar hour angle $\omega$:

$$\sin\alpha_s = \cos Z = \sin\phi\sin\delta + \cos\phi\cos\delta\cos\omega \tag{20}$$

$$\psi_s = \text{sign}(\omega)\left[\cos^{-1}\left(\frac{\cos\delta\cos\omega - \cos Z\cos\phi}{\sin Z\sin\phi}\right)\right] \tag{21}$$

4.6.3. Angle of Incidence

Usually, the infrastructure boundaries are tilted against the horizontal surface. The tilt is described by the tilt angle $Y$ against the horizontal plane, which varies in the range of $0 \leq Y \leq 180°$.

The incident angle $\alpha$ of the beam radiation on a tilted surface of any orientation is expressed in terms of the surface angle $Y$, the Sun's declination $\delta$, the Earth's latitude $\phi$, the solar hour angle $\omega$ and the azimuth $\psi$ [23]:

$$\cos\alpha = A\sin\delta + B\cos\omega\cos\delta + C\sin\omega\cos\delta \quad (22)$$

with

$$\begin{aligned} A &= \cos Y\sin\phi - \sin Y\cos\phi\cos\psi \\ B &= \cos Y\cos\phi + \sin Y\sin\phi\cos\psi \\ C &= \sin Y\sin\psi \end{aligned} \quad (23)$$

If the right-hand side of Equation (22) is negative, the Sun's rays do not strike the front side of the surface and therefore, it is shaded.

#### 4.6.4. Solar Radiation Components

According to the Liu–Jordan theory [24], the solar radiation $I_T$ that reaches a surface tilted at an angle $Y$ (in reference to a horizontal plane) is described by the equation:

$$I_T(t) = I_b(t)R_b(t) + I_d(t)R_d + [I_b(t) + I_d(t)]\rho_o R_r \quad (24)$$

where $I_b$ and $I_d$ are, respectively, the beam and the diffuse radiation intersecting on a horizontal surface, $\rho_o$ is the surface (ground) reflectance, and $R_b$, $R_d$, and $R_r$ are, respectively, the correction factors for the beam, diffuse, and reflected radiation

$$R_b = \frac{\cos\alpha}{\cos Z} \quad (25)$$

$$R_d = \frac{1+\cos Y}{2} \quad (26)$$

$$R_r = \frac{1-\cos Y}{2} \quad (27)$$

#### 4.6.5. Solar Irradiance

The average solar irradiance at the site where the dam was located can be represented by the average solar radiation measured at the Penhas Douradas station given by [25,26]:

$$I_b = I_o \exp(-0.968 + 0.760\cos Z)\cos Z \quad (28)$$

where $I_o$ is the solar constant (1367 W/m$^2$). In fact, the solar irradiance measured at the solar radiation station corresponds to the global horizontal irradiation, which is the sum of the beam and diffuse radiation. However, as no data are available to decompose the radiation, all measured irradiance was considered as beam radiation, and the diffuse radiation was neglected.

It is also worth noting that the function represents average measured values, that is, already affected by average cloud-cover conditions. The absorption coefficient was set to 0.65 for the dam and the spillway. No solar radiation was considered for the rock foundation in order to take into account the vegetation cover.

#### 4.6.6. Shading of Beam Radiation

It can be observed from Figure 8 that self- and external obstructions can prevent the direct component of the light from reaching the dam faces. Therefore, it is important to determine which part of the dam's faces is shaded at any particular time to correctly predict the solar radiation flux.

From the pioneering work of Jin et al. [27] to most recent works [28,29], authors have used the ray-tracing algorithm to define the shaded area caused by the surrounding terrain and the dam itself. An exception is the work of Santillán and coworkers, who computed the

shading of the dam by recourse to the projection of the different surfaces in the direction of the sunrays [30,31]; however, later on, they also adopted the ray-tracing algorithm [32,33].

The basic idea of the ray-tracing technique is to start a ray at the object and send it to the sun. If this backward ray reaches the sun without hitting any object along its way, then the beam radiation strikes the object, otherwise, it is in the shadow. The problem of the intersection of a ray with an object is one of the classical problems in the field of computer graphics, where many algorithms for ray tracing have been developed. For this work, the ray-triangle intersection algorithm presented in [34] was adopted.

### *4.7. Preliminary Results*

The transient thermal analysis was performed with the same version of the in-house code PAT used in [11]. This code applies a fully implicit Euler backward finite difference scheme for the time discretization and a finite element scheme for the spatial discretization. The analysis was conducted considering an incremental time of 1 h.

Before addressing the whole thermo-mechanical results in Section 6, some previous interesting analysis is presented.

On the one hand, in order to analyze the uneven distribution of the received solar irradiation along the downstream face of the dam, the concept of daily and annual solar irradiance was used. In this sense, the total amount of solar irradiance for one day or for the year was calculated by integrating (i.e., summing) the individual hourly solar irradiance values obtained within the corresponding period. Figure 9 illustrates the values obtained for the daily solar irradiation on the downstream face at the winter and summer solstices and at the equinoxes.

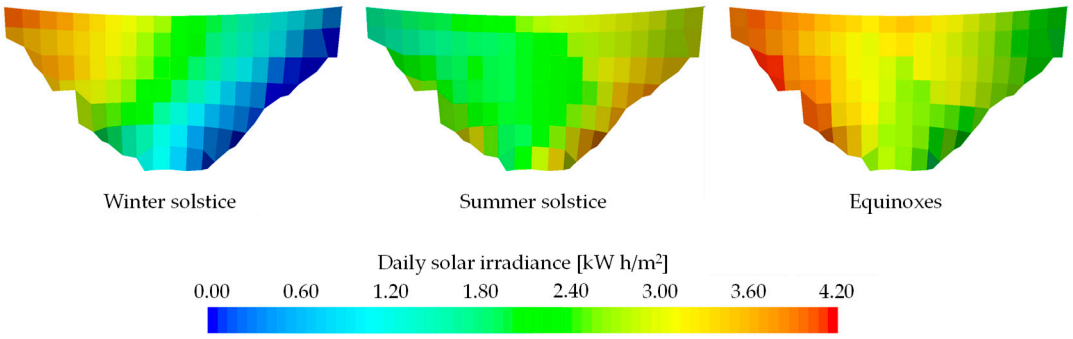


**Figure 9.** Daily solar irradiance calculated at the solstices and equinoxes over the downstream face of the dam.

As can be seen, the right flank of the dam received much more sunshine than the left flank from autumn to spring. As a result of that, the total annual irradiance received by the right flank of the downstream face of the dam was more than twice as large as the amount received by the left flank, Figure 10.

On the other hand, due to the lack of thermal monitoring and in an attempt to validate the numerical results, a comparison between the image obtained by a thermal survey and the corresponding FEM values are shown in Figure 11.

The thermal survey was carried out by LNEC two weeks before the demolition of the dam, on 4 June 2013 at approximately 3 p.m. The object of the thermal survey was to evaluate the suitability of a thermal camera to detect resurgences of water on the downstream surface of dams [35]. For the survey, the camera was mounted on a tripod placed on the left bank and 26 images were recorded. Later, these images were stitched, creating the panoramic image represented in the figure. Although there is no associated color scale, the blue color corresponds to cold areas, the red color corresponds to hot areas, and the white color is reserved for the hottest areas.

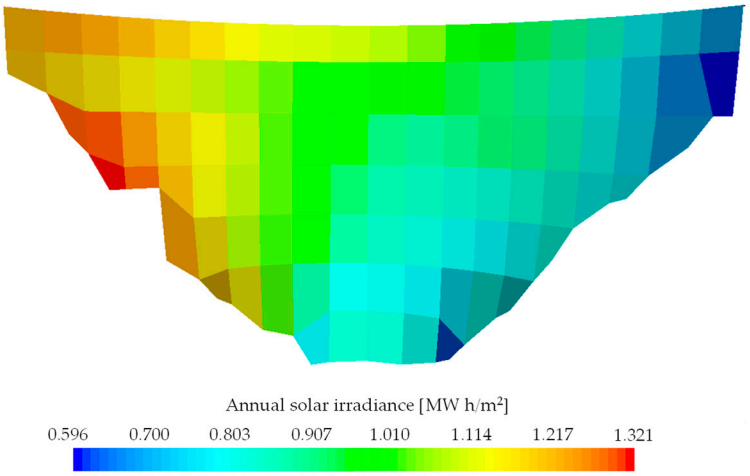


**Figure 10.** Annual solar irradiance over the downstream face of the dam.

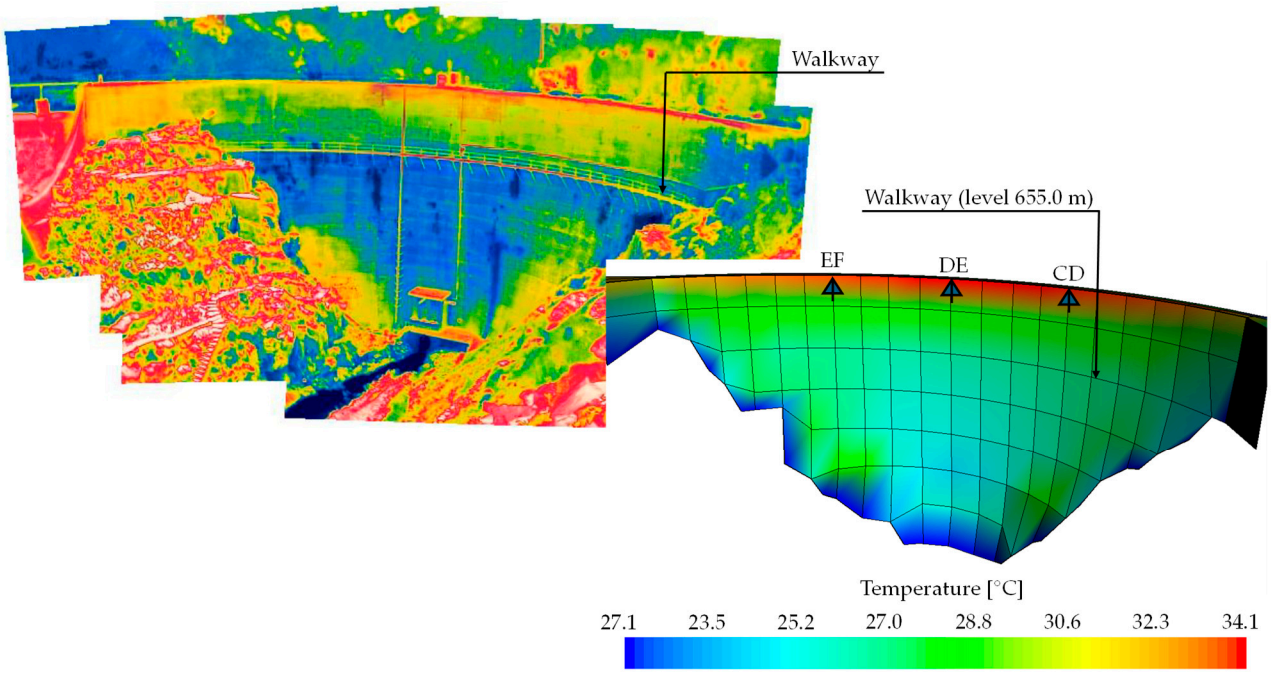


**Figure 11.** Thermal panoramic image and FEM simulation on 4 June at 3 p.m.

The FEM results correspond to the temperature distribution obtained for the 4 June at 3 p.m., the day and time of the thermal survey. As can be inferred from Figure 8, near the summer solstice, the sun at 3 p.m. is further west than the one represented in the picture. In that position, the sun strikes the downstream face of the dam in an almost symmetric way.

It is worth noting that the numerical simulation used average values of the thermal actions. However, in spite of the variability of the air temperature, nebulosity, and wind speed, it is still possible to recognize a close resemblance between the two images. Both of them show a hotter zone above the walkway located at level 655.0 m, with the maximum near the crest, and a cooler zone below the walkway with an increment of the temperature from the center of the dam to the abutments.

## 5. Mechanical Analysis

### *5.1. General Remarks*

The structural problem was solved incrementally through time, considering a time step of 2 weeks. The analysis was carried out with the code PAVK developed by the

author. With a view to covering concrete dam analysis, this code was provided with a library of selected elements, material models, and load cases appropriate for that purpose. The element library comprises 2D and 3D elements, to represent the concrete and the rock foundation, and interface elements, to represent the contraction joints and the dam–foundation interface [26].

For the concrete, masonry, and rock, an elastic behavior was adopted. The only non-linear behavior considered was the one introduced by the representation of the contraction joints and the dam–foundation interface. The elasticity moduli adopted were 30 GPa for the concrete and 20 GPa for the masonry and the rock mass, and all the Poisson coefficients were set to 0.2.

A zero normal displacement boundary condition was imposed at the bottom and lateral boundaries of the rock mass foundation.

The analysis began with all the contraction joints open, i.e., without any interaction between two consecutive blocks. In this way, it was possible to simulate the installation of the dead load on the cantilever monoliths prior to the grouting of the contraction joints. In the next step, the displacements were reset to zero, simulating the grouting of the contraction joints, and the corresponding interface elements were activated. At that stage, the hydrostatic pressure on the upstream face of the dam was applied. After that, the hydrostatic pressure was maintained unchanged at a level of 660.0 m, and thermal and AAR expansions were applied for the period from 13th March 1950, date of the first geodetic survey, to 31st December 1978.

### *5.2. Thermal Load*

Since no construction records were available, the reference (closure) temperature had to be adopted in order to calculate the temperature load. In this regard, the criterion adopted in [36], which considered a uniform reference temperature equal either to the mean annual concrete temperature or to the mean annual air temperature, was considered unrealistic because concrete temperatures always present a spatial distribution [17]. Instead, it was assumed as reference the temperatures obtained for the 27th of April, which is the day when the annual harmonic function reaches the mean temperature.

### *5.3. AAR Model*

According to [37], the incremental volumetric AAR expansion strain is given by:

$$\dot{\varepsilon}_V^{AAR}(t,T) = \Gamma_t \, \Gamma_c \, g(h) \, \dot{\xi}(t,T) \, \varepsilon(\infty) \tag{29}$$

where $0 \leq \Gamma_t \leq 1$ is a parameter which reduces the expansion in the presence of large tensile stresses (macro-cracks absorbing the gel); $0 \leq \Gamma_c \leq 1$ is a parameter which accounts for the absorption of the gel due to compressive induced stresses; $0 \leq g(h) \leq 1$ is a function of the relative humidity (set to zero if the humidity is below 80%); $\dot{\xi}(t,T)$ is the rate form of the kinetics law; and $\varepsilon(\infty)$ is the final volumetric expansion.

The swelling process evolution is taken into account by the kinetics law proposed by Larive [38]:

$$\xi(t,T) = \frac{1 - e^{-\frac{t}{\tau_c(T)}}}{1 + e^{-\frac{t-\tau_l(T)}{\tau_c(T)}}} \tag{30}$$

or in rate form:

$$\dot{\xi}(t,T) = \frac{e^{t/\tau_c}\left(e^{\frac{\tau_l}{\tau_c}} + 1\right)}{\tau_c\left(e^{t/\tau_c} + e^{\frac{\tau_l}{\tau_c}}\right)^2} \tag{31}$$

where $\tau_l$ and $\tau_c$ are the latency and characteristic times, respectively, corresponding to the initiation and the development period of AARs from a practical point of view. Both time parameters depend on the temperature and the relative humidity. If only the temperature factor is taken into account, the dependence was proposed in the form:

$$\tau_l(T) = \tau_l(T_o)\exp\left[U_l\left(\frac{1}{T} - \frac{1}{T_o}\right)\right] \tag{32}$$

$$\tau_c(T) = \tau_c(T_o)\exp\left[U_c\left(\frac{1}{T} - \frac{1}{T_o}\right)\right] \tag{33}$$

where $T$ is the temperature, $T_o$ = 38 °C is the reference temperature, and $U_l$ and $U_c$ are the Arrhenius activation energies ($U_l = 9400 \pm 500$ $K$ and $U_c = 5400 \pm 500$ $K$).

The factor that accounts for the reduction in the rate of volumetric AAR expansion under compressive stresses was adopted following the work of Liaudat et al. [39]:

$$\Gamma_c = \begin{cases} 1 & \text{if} \quad \sigma_v \geq 0 \\ 1 - \left(\frac{\sigma_v}{\overline{\sigma_v}}\right)^2 & \text{if} \quad 0 > \sigma_v \geq \overline{\sigma_v} \\ 0 & \text{if} \quad \sigma_v < \overline{\sigma_v} \end{cases} \tag{34}$$

where $\sigma_v$ is the volumetric stress defined as $\sigma_v = (\sigma_I, \sigma_{II}, \sigma_{III})/3$, $(\sigma_I, \sigma_{II}, \sigma_{III})$ are the principal stresses, and $\overline{\sigma_v}$ is a parameter that stands for the volumetric stress under which AAR expansion would be totally suppressed, taken as −9.7 MPa.

Since the present study was limited to exploring the influence of the nonuniform temperature distribution due to solar radiation and shading, a simplified version of Equation (29) was used in which the factors $\Gamma_t$ and $g(h)$ were set to one. Therefore, the reduction in the free volumetric AAR expansion due to large tensile stresses and humidity were not considered in this work. These specific effects will be further explored in future studies.

At each new time step $t_{i+1} = t_i + \Delta t$, the increment of the swelling $\Delta\xi$ was computed as:

$$\Delta\xi = \dot{\xi}(t^*, T)\Delta t \tag{35}$$

where $t^* = t_i + \Delta t/2$, and $\Gamma_c$ was computed using the stress state obtained at the beginning of the interval.

Once the volumetric AAR strain was determined, it was decomposed into a tensorial strain in accordance with the three weight factors associated with the principal stresses by means of the formula given in [40] as follows:

$$\dot{\varepsilon}_i^{AAR}(t, T) = W_i(\sigma_I, \sigma_{II}, \sigma_{III})\dot{\varepsilon}_V^{AAR}(t, T) \tag{36}$$

where $\dot{\varepsilon}_i^{AAR}$ is the AAR expansion rate in the principal axis $i$, and $W_i$ is a weight factor for the principal axis $i$, which is a function of the principal stresses. This weight factor was calculated following the procedure proposed by Souma and Perotti [40], except for $\sigma_u \leq \sigma_{l/m} \leq f'_c$, in which case $\sigma_{l/m} = \sigma_{l/m} - \sigma_u$ was adopted instead of $\sigma_{l/m} = f'_c - \sigma_{l/m}$, as indicated in [40], to be consistent with the bilinear shape function interpolation.

Finally, a coordinate transformation was applied to the $\dot{\varepsilon}_i^{AAR}$ tensor from the principal axis to the global axis using the principal direction matrix.

### *5.4. Discontinuities Modelling*

Concrete arch dams are constructed as a system of monolithic blocks separated by contraction joints. The monoliths are constructed separately so that cooling and shrinkage may take place independently in each one. After the construction period, the contraction joints are grouted under high pressure with the aim of forming a complete monolithic structure. However, contrary to the conventional view that grouting of contraction joints brings a monolithic behavior to dams, contraction joints continue working through the entire dam's lifespan since grouted joints can take little or no tension [41,42].

Additionally, high tensile stresses can be expected to occur mainly at the upstream heel due to the water load exerted by the reservoir, leading to crack formation. These cracks are usually stable, as long as shear stresses do not exceed the shear strength of mass concrete

and rock. However, if a crack at the base of a dam opens, the deformations of the dam will increase, resulting in a redistribution of the stresses, thus increasing the arch stresses.

To capture the influence of such discontinuities, zero-thickness interface elements were placed along the contraction joints and the dam–foundation interface. In this approach, the contact constraint was enforced by the penalty method, where the normal stiffness $k_n$ and the tangential stiffnesses $k_s$ and $k_t$ played the role of penalty coefficients. This meant that they had to be set as high as possible to guarantee that no penetration took place while joints were closed, but not so high as to avoid ill-posed problems. In this way, the normal and tangential stiffness had no physical meaning, and therefore, no additional material parameter was required. Moreover, no-tension and no-sliding conditions were assumed to characterize the normal and tangential behaviors, respectively, which also avoided the need for extra material parameters.

## 6. Results

The thermo-mechanical analysis was run from 13th March 1950, date of the first geodetic survey, to 31st December 1978, when the level of cracking was incompatible with the assumption of a linear behavior of the concrete. For a generic year, the considered dates were 15 January, 29 January, 12 February, 26 February, 12 March, 26 March, 9 April, 23 April, 7 May, 21 May, 4 June, 18 June, 2 July, 16 July, 30 July, 13 August, 27 August, 10 September, 24 September, 8 October, 22 October, 5 November, 19 November, 3 December, 12 December, and 31 December. In general, all the intervals lasted two weeks with the exception of the interval between 31st of December and 15th of January, and in leap years, the interval between 21 February and 12 March, which lasted 15 days. In all cases, the temperatures obtained at midday (12:00 local time) were considered.

In order to compute the volumetric AAR expansion, 4.5 years and 4 years were adopted for the latency and characteristic times, respectively, and 0.0045 for the final volumetric expansion.

In order to investigate the influence of the solar radiation and the associated shadow effect, the same thermo-mechanical analysis was carried out without considering the sun's rays striking the dam. Graphical comparisons of both models are presented in Figures 12–17.

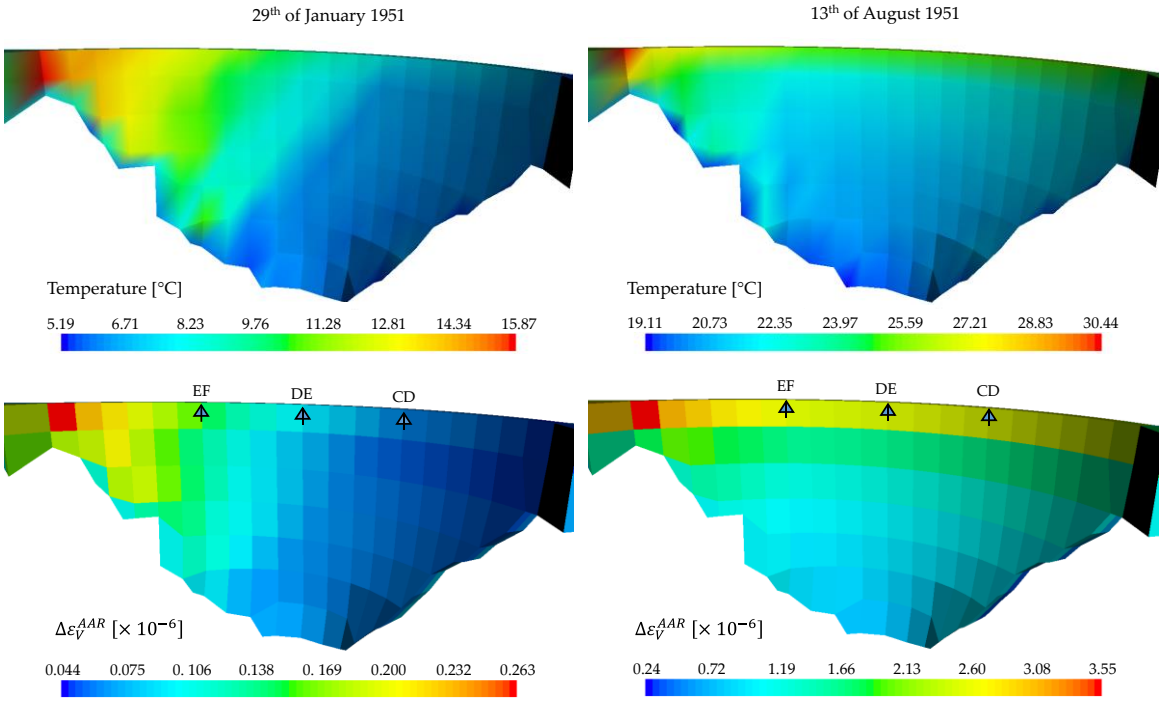


**Figure 12.** Temperature and volumetric AAR expansion increment calculated on 29 January and 13 August 1951, considering solar radiation.

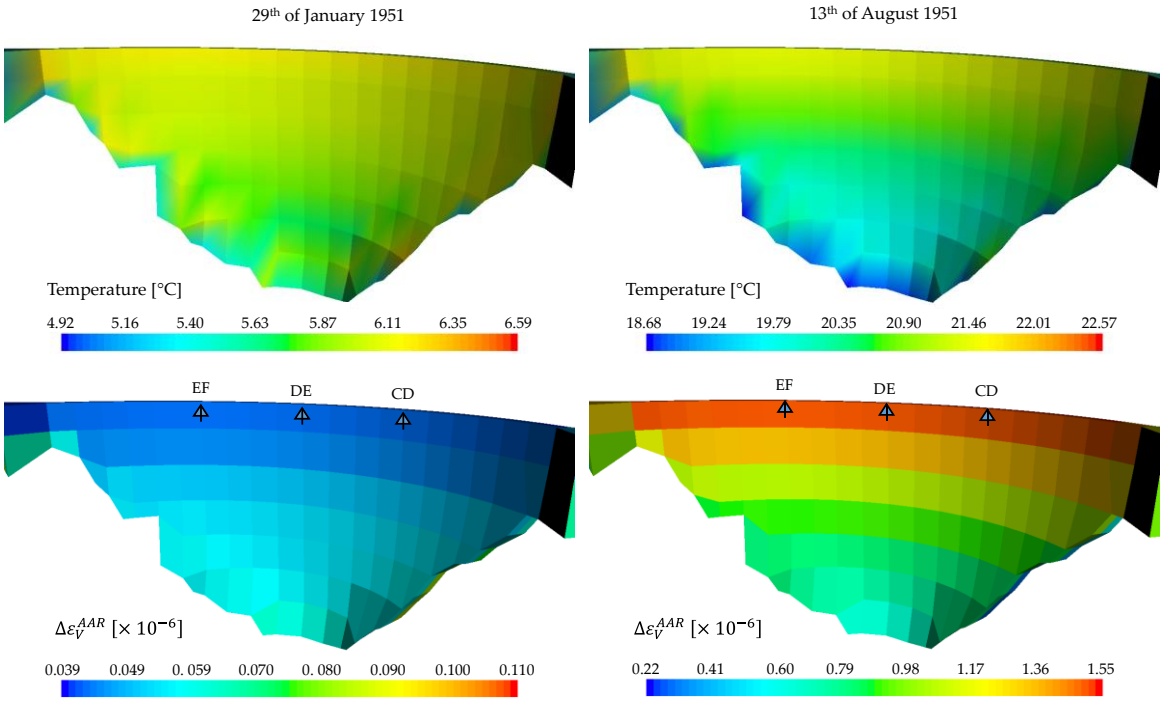


**Figure 13.** Temperature and volumetric AAR expansion increment calculated on 29 January and 13 August 1951, without considering solar radiation.

Figures 12 and 13 illustrate the values of the temperatures and the two-week increment of the volumetric AAR expansion obtained on 29 January and 13 August 1951, when considering the solar radiation effect or not, respectively.

As mentioned before, once the volumetric AAR strain was determined, it was decomposed into a tensorial strain in accordance with the three weight factors associated with the principal stresses, and after that, they were rotated from the principal axis to the global axis in order to compute the increment of displacement.

In Figures 14 and 15, the displacements computed on 13 March, date of the first geodetic survey, and on 12 March every four years are presented. In this figure, the color contour plot represents the total displacement, and the deformed mesh is represented with a scale factor of 200. Additionally, in order to help the comparison, the deformed mesh computed in 1950 is superposed in each picture. It should be recalled that the zero position was defined for an empty reservoir and for the temperatures registered on 27 April, adopted as reference temperatures.

Finally, in Figures 16 and 17, the radial and vertical displacement evolution obtained with the numerical model considering the solar radiation effect (solid line), or without considering the solar radiation effect (dotted line) and the measured values (discrete points) are compared. For these representations, the zero displacement corresponds to the one computed on 12 March 1950.

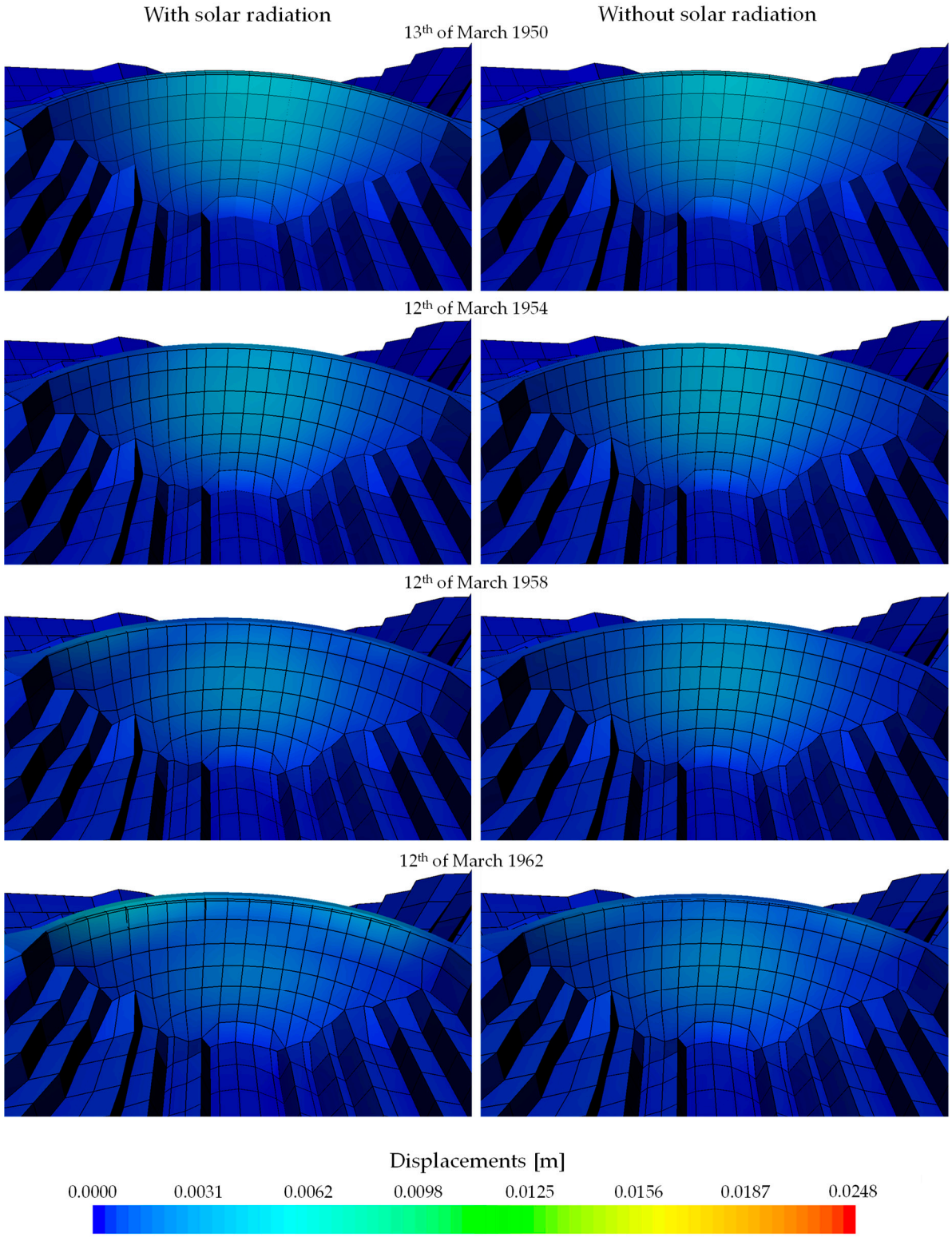


**Figure 14.** Displacement contour plots calculated from 13 of March 1950 to 12 March 1962.

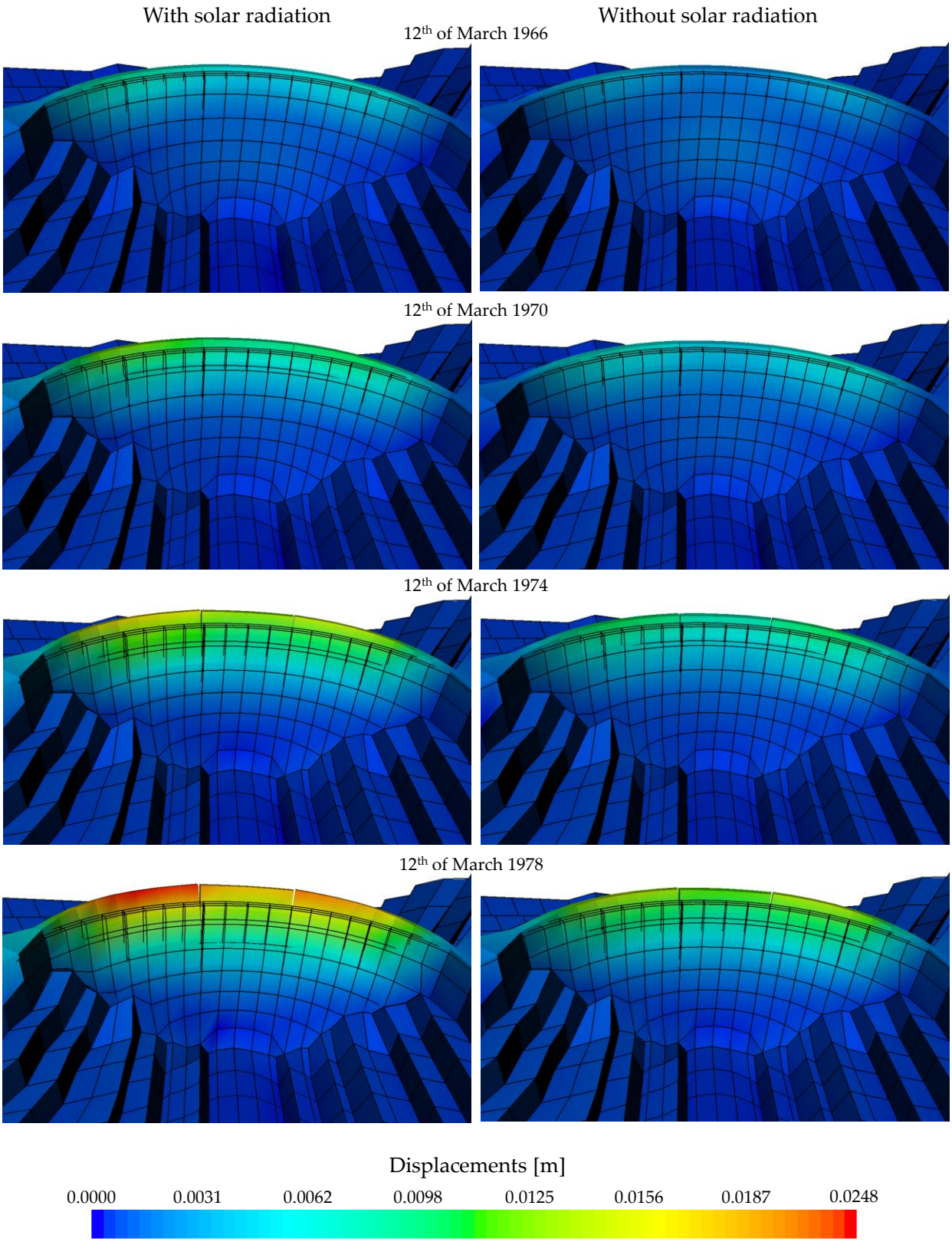


**Figure 15.** Displacement contour plots calculated on 12 March from 1966 to 1978.

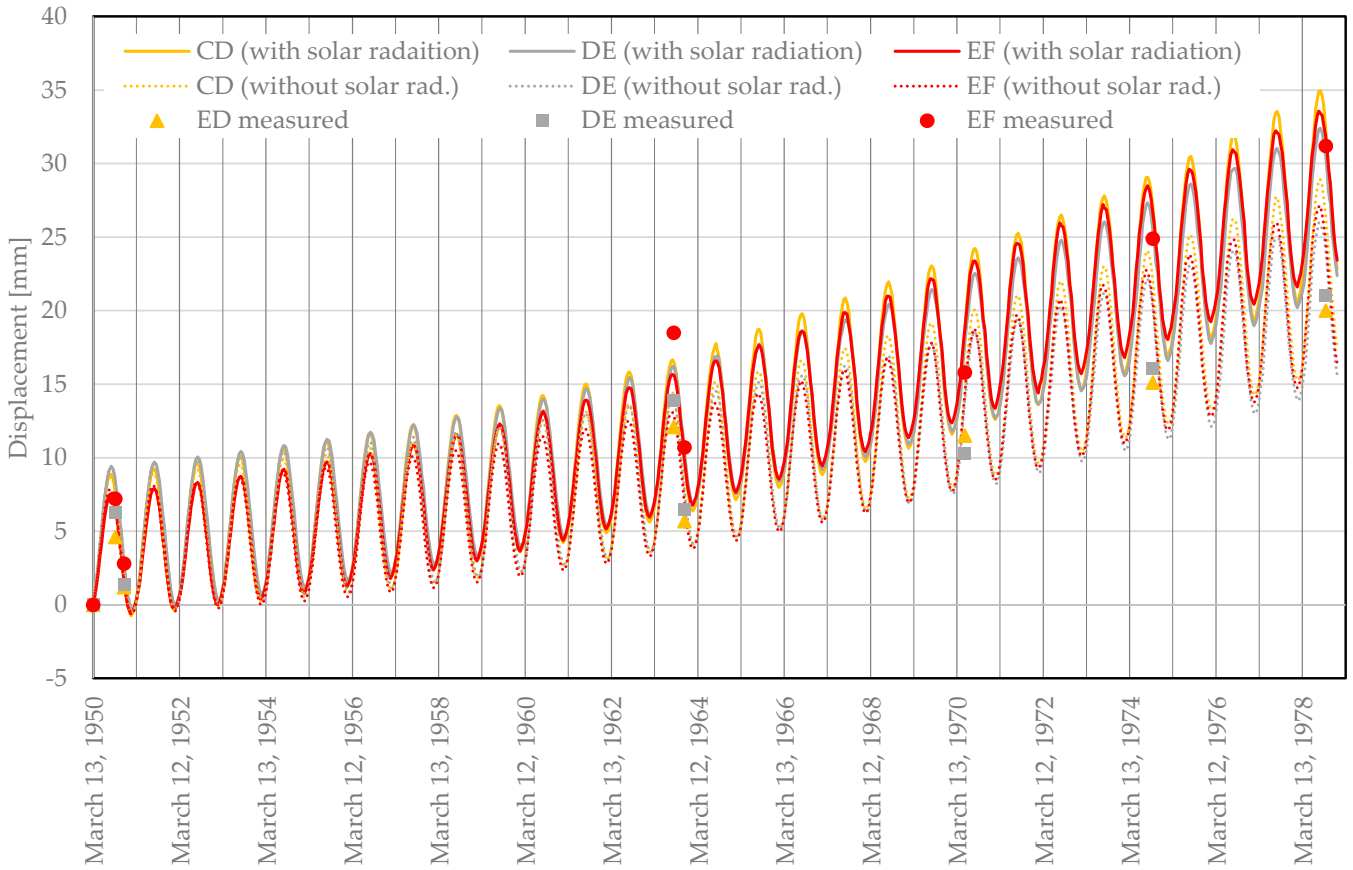


**Figure 16.** Radial displacements evolution from 1950 to 1978 for the object points CD, DE, and EF at level 663.0 m.

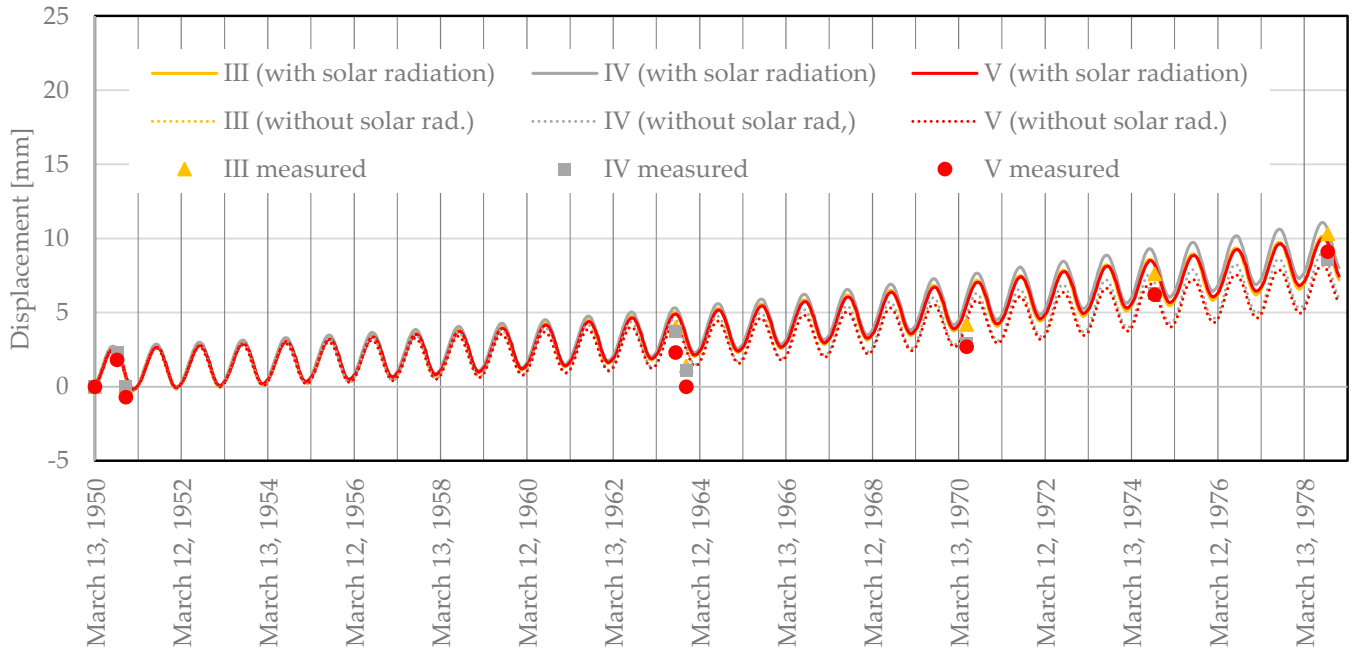


**Figure 17.** Vertical displacements evolution from 1950 to 1978 for the object points III, IV, and V.

## 7. Discussion

By analyzing Figure 12, which represents the model considering the solar radiation effect, it is possible to observe the influence of the downstream temperatures on the volumetric AAR expansion. In contrast, in the case when no solar radiation effect is considered, represented in Figure 13, a stratified distribution of the volumetric AAR expansion is observed. To interpret this behavior, it is worth noting that temperature is a primary variable and, consequently, it is computed at each node, whereas the strain (in this case the AAR expansion) is a secondary variable, and it is computed at the integration point level. Therefore, the values of AAR expansions not only depend on the temperature computed at the downstream face of the dam but on the temperatures obtained at the 20 nodes of each element.

In this way, when the downstream face presents an approximately uniform temperature, the differences in the volumetric AAR expansion are dictated by the temperatures of the upstream face of the dam. This is the case when no solar radiation effect is considered (Figure 13). During winter, when the water temperature is slightly warmer at the bed of the reservoir, the volumetric AAR expansions become larger at the bottom and gradually decrease towards the crest of the dam. On the contrary, during summer, when the water temperature decreases with increasing depth, the volumetric AAR expansions are larger at the crest and decrease toward the base of the dam.

It is also important to note that the volumetric AAR expansion represented in the figure corresponds to the average value of the expansion computed at each integration point of the element. Analyzing these results, it should be noted that the difference between values computed in different elements at the same time of the year or from the same element but at different times of the year might differ by one order of magnitude.

Figures 14 and 15 show the deformation of the dam induced by the AAR expansion. In this respect, it is worth pointing out that in the first picture of Figure 14, representing the displacements computed in 1950, the dam had moved downstream due to the effects of the water pressure and of the temperature decrease in relation with the reference temperature. The maximum displacement was computed at the center of the dam and had a value of 0.00480 m. After that, since the water level was kept constant and the temperature varied in a cyclical manner, the difference in behavior was only due to the AAR expansions, which induced displacements in the upstream and upward directions. In 1954, the maximum value had diminished to 0.00377 m and 0.00403 m, for the model considering the solar radiation effect or not, respectively. For the model considering the solar radiation effect, eight years later, in 1958, the displacements near the crest at both sides of the dam began to show a greater increase than the displacements computed at the center of the dam, with greater values on the right side. The same behavior took another eight years to appear in the model without considering the solar radiation effect (Figure 15). By the year 1970, it was also possible to note that the central contraction joints had begun to open in both models. During the following eight years, the model with solar radiation began to show a slight increase in the displacements of the right side compared with the left side of the dam. Instead, the model without solar radiation continued to present an almost symmetrical behavior.

Regarding the evolution of the radial displacements, as seen in Figure 16, the consideration of the solar radiation effect accelerated the rate of expansion. It can also be observed in that model that point EF presented the highest and the middle point presented the lowest rate of expansion. However, compared with the measured radial displacements, the model overestimated the rate for points DE and EF.

About the evolution of the vertical displacements, shown in Figure 17, the model in general followed the rate of growth observed in the geodetic survey of the vertical displacements. However, in 1963, some discrepancies that warrant further study could be observed.

From the above analysis, it is clear that the model considering the solar radiation effect can reproduce the heterogeneity of the AAR expansion distribution, as seen in Figure 12.

However, due to the order of magnitude of these expansions, this heterogeneity is diluted at the displacement level, showing that Expressions (31) to (33) warrant further investigation in order to obtain a better representation.

## 8. Conclusions

Two thermal-mechanical analyses were carried out using a nonlinear mechanical model for a dam, taking into account the seasonal temperature variation in the air and reservoir water temperature. In one of the models, the spatiotemporal distribution of the solar radiation incidence on the dam surfaces and shading were also considered. The comparison of the results allows us to conclude the following:

- Solar radiation contributes to the uneven development of AAR expansion, introducing a difference of up to one order of magnitude between the side exposed to the sun's rays and the shady side.
- Simplified solar radiation models should be avoided in order to obtain a representative distribution of the AAR expansion.
- As an AAR evolves, the displacements in the upstream direction tend to open the contraction joints. Hence, the representation of the contraction joints is unavoidable in the mechanical analysis.

Finally, it is worth mentioning that it is an ongoing study. Therefore, some issues still warrant further investigation in order to obtain a better representation.

**Funding:** This research received no external funding.

**Institutional Review Board Statement:** Not applicable.

**Informed Consent Statement:** Not applicable.

**Data Availability Statement:** The thermal analysis code used in this study is available at https://github.com/nschclar/PAT (see folder PAT_V1_3 for the later version of PAT).

**Conflicts of Interest:** The author declares no conflicts of interest.

## References

1. ICOLD. *Alkali-Aggregate Reaction in Concrete Dams—Review and Recommendations*; Bulletin 79; Commission Internationale des Grands Barrages: Paris, Prance, 1991.
2. Fournier, B.; Ideker, J.H.; Folliard, K.J.; Thomas, M.D.A.; Nkinamubanzi, P.; Chevrier, R. Effect of environmental conditions on expansion in concrete due to alkali–silica reaction (ASR). *Mater. Charact.* **2009**, *60*, 669–679. [CrossRef]
3. Amberg, F.; Droz, P.; Leroy, R.; Maier, J.; Otto, B.; Bremen, R. *Concrete Swelling of Dams in Switzerland*; Report of the Swiss Committee on Dam on the state of concrete swelling in Swiss Dams; Switzerland, 2017. Available online: https://www.swissdams.ch/fr/publications/publications-csb/2017_Concrete%20swelling.pdf (accessed on 1 March 2024).
4. Amberg, F. Performance of dams affected by expanding concrete. In *Dams and Reservoirs under Changing Challenges*; Schleiss, A., Boes, R., Eds.; Taylor & Francis Group: London, UK, 2011; pp. 115–122.
5. Saouma, V.; Perotti, L.; Shimpo, T. Stress analysis of concrete structures subjected to alkali-aggregate reactions. *ACI Struct. J.* **2007**, *104*, 532–541. [CrossRef]
6. Saouma, V.E.; Hariri-Ardebili, M.A. *Aging, Shaking, and Cracking of Infrastructures, from Mechanics to Concrete Dams and Nuclear Structures*; Springer: Cham, Switzerland, 2021.
7. Stucchi, R.; Catalano, E. Numerical modelling of the Pian Telessio dam affected by AAR. In *Role of Dams and Reservoirs in a Successful Energy Transition*, 1st ed.; Boes, R., Droz, P., Leroy, R., Eds.; Taylor & Francis: London, UK, 2023; pp. 964–971.
8. Lombardi, G.; Amberg, F.; Darbre, G.R. *Algorithm for the Prediction of Functional Delays in the Behaviour of Concrete Dams*; Lombardi Engineering Limited: Bellinzona, Switzerland, 2006.
9. Lamea, M.; Mirzabozorg, H. Evaluating sensitivity of an AAR-affected concrete arch dam to the effects of structural joints and solar radiation. *Strength Mater.* **2015**, *47*, 341–354. [CrossRef]
10. Leitão, N.S.; Castilho, E. Heat transfer analysis of infrastructures subjected to environmental actions: A finite element solver PAT. *Therm. Sci. Eng. Prog.* **2022**, *34*, 101447. [CrossRef]
11. Leitão, N.S.; Oliveira, S. Insights about Modelling Environmental Spatiotemporal Actions in Thermal Analysis of Concrete Dams: A Case Study. *Thermo* **2023**, *3*, 605–624. [CrossRef]
12. Ramos, J.M.; Batista, A.L.; Oliveira, S.B.; de Castro, A.T.; Silva, H.M.; de Pinho, J.S. Reliability of arch dams subject to concrete swelling: Three cases histories. In Proceedings of the 2nd International Conference on Alkali-Aggregate reaction in Hydraulic Plants and Dams, Chattanooga, TN, USA, 22–27 October 1995.

13. Oliveira, S.B.; Pina, C.A.; Ramos, J.M.; Tavares de Castro, A. *Assessment of the Behaviour of the Alto Ceira Dam. Structural Safety Evaluation*; Internal LNEC Report; Laboratório Nacional de Engenharia Civil: Lisbon, Portugal, 1995. (In Portuguese)
14. Reis, M.O.; Silva, H.S.; Silva, A.S. AAR in Portuguese structures, some case histories. In Proceedings of the 10th International Conference on Alkali-Aggregate Reaction in Concrete, Melbourne, Australia, 18–23 August 1996.
15. Schclar Leitão, N.; Tavares de Castro, A. *Evaluation of Alto Ceira Dam Structural Safety*; Internal LNEC Report; Laboratório Nacional de Engenharia Civil: Lisbon, Portugal, 2004. (In Portuguese)
16. Braga Farinha, M.L. *Alto Ceira Dam. Assessment of the Cracking Using Ultrasound Test*; Internal LNEC Report; Laboratório Nacional de Engenharia Civil: Lisbon, Portugal, 2004. (In Portuguese)
17. Salazar, F.; Vicente, D.J.; Irazábal, J.; de-Pouplana, I.; San Mauro, J. A review on thermo-mechanical modelling of arch dams during construction and operation: Effect of the reference temperature on stress field. *Arch. Comput. Methods Eng.* **2020**, *27*, 1681–1707. [CrossRef]
18. Çengel, Y.A. *Heat Transfer: A Practical Approach*, 2nd ed.; McGraw-Hill Education—Europe: London, UK, 2002.
19. USACE. *Thermal Studies of Mass Concrete Structures*; Technical Letter No. 1110-2-542; U.S. Army Corps of Engineers: Washington, DC, USA, 1997.
20. Bofang, Z. *Thermal Stresses and Temperature Control of Mass Concrete*, 1st ed.; Butterworth-Heinemann: Oxford, UK, 2014.
21. ASHRAE. *2009 ASHRAE Handbook: Fundamentals*, SI ed.; American Society of Heating, Refrigerating and Air-Conditioning Engineers, Inc.: Atlanta, GA, USA, 2009.
22. Spencer, J.W. Fourier series representation of the position of the sun. *Search* **1971**, *2*, 162–172.
23. Chwieduk, D. *Solar Energy in Buildings: Thermal Balance for Efficient Heating and Cooling*; Academic Press: Oxford, UK, 2014.
24. Liu, B.Y.H.; Jordan, R.C. The long-term average performance of flat-plate solar-energy collectors. *Sol. Energy* **1963**, *7*, 53–74. [CrossRef]
25. Silveira, A. *Temperatures Variations in Dams*; LNEC: Lisbon, Portugal, 1961. (In Portuguese)
26. Leitão, N.S.; Castilho, E.; Farinha, M.L.B. Towards a Better Understanding of Concrete Arch Dam Behavior during the First Filling of the Reservoir. *CivilEng* **2023**, *4*, 151–173. [CrossRef]
27. Jin, F.; Chen, Z.; Wang, J.; Yang, J. Practical Procedure for Predicting non-uniform Temperature on the Exposed Face of Arch Dams. *Appl. Therm. Eng.* **2010**, *30*, 2146–2156. [CrossRef]
28. Pan, J.; Liu, W.; Wang, J.; Jin, F.; Chi, F. A novel reconstruction method of temperature field for thermomechanical stress analysis of arch dams. *Measurement* **2022**, *188*, 110585. [CrossRef]
29. Shao, C.; Zhao, E.; Xu, Y.; Zheng, S.; Tian, S. Genesis Analysis of Special Deformation Characteristics for Super-High Arch Dams in the Alpine and Gorge Regions of Southwest China. *Mathematics* **2023**, *11*, 1753. [CrossRef]
30. Santillán, D. Mejora de los Modelos Térmicos de las Presas Bóveda en Exploración. Aplicación al Análisis del Efecto del Cambio Climático [Improvement of the Thermal Models of Arch Dams in Operation. Application to the Analysis of the Climate Change Effect]. Ph.D. Thesis, Polytechnic University of Madrid, Madrid, Spain, 2014.
31. Santillán, D.; Salete, E.; Vicente, D.; Toledo, M. Treatment of Solar Radiation by Spatial and Temporal Discretization for Modelling the Thermal Response of Arch Dam. *J. Eng. Mech.* **2014**, *140*, 05014001. [CrossRef]
32. Santillán, D.; Salete, E.; Toledo, M. A Methodology for the Assessment of the Effect of Climate Change on the Thermal-strain-stress Behaviour of Structures. *Eng. Struct.* **2015**, *92*, 123–141. [CrossRef]
33. Belkmore, A.; Mihoubi, M.; Santillán, D. Analysis of Dam Behavior by Statistical Models: Application of the Random Forest Approach. *KSCE J. Civ. Eng.* **2019**, *23*, 4800–4811. [CrossRef]
34. Scratchapixel 3.0, Ray-Tracing: Rendering a Triangle. Available online: https://www.scratchapixel.com/index.html (accessed on 6 July 2023).
35. Henriques, M.J.; Ramos, P. Thermal Imaging of Concrete Dam Surfaces to Support the Control of the Evolution of Pathologies. In Proceedings of the Second International Dam World Conference, Lisbon, Portugal, 21–24 April 2015.
36. FERC. Chapter 11: Arch Dams. In *Engineering Guidelines for the Evaluation of Hydropower Projects*; Federal Energy Regulatory Commission: Washington, DC, USA, 1999.
37. Saouma, V. *Numerical Modeling of AAR*, 1st ed.; CRC Press/Balkema: Leiden, The Netherlands, 2014.
38. Larive, C. Apports Combinés de L'expérimentation et de la Modélisation à la Compréhension de L'alcali-Réaction et de ses Effets Mécaniques. Ph.D. Thesis, Ecole Nationale des Ponts et Chaussées, Champs-sur-Marne, France, 1997.
39. Liaudat, J.; Carol, I.; Lopez, C.; Saouma, V. ASR expansions in concrete under triaxial confinement. *Cem. Concr. Compos.* **2018**, *86*, 160–170. [CrossRef]
40. Saouma, V.; Perotti, L. Constitutive Model for Alkali-Aggregate Reactions. *ACI Mater. J.* **2006**, *103*, 194–202. [CrossRef]
41. Boggs, H.L.; Jansen, R.B.; Tabox, G.S. Arch Dam Design and Analysis. In *Advanced Dam Engineering for Design, Construction, and Rehabilitation*; Jansen, R.B., Ed.; Springer: Boston, MA, USA, 1988; pp. 493–539. [CrossRef]
42. FERC. Chapter 11: Arch Dams. In *Engineering Guidelines for the Evaluation of Hydropower Projects*; Federal Energy Regulatory Commission: Washington, DC, USA, 2018.